Open Ceramics 15 (2023) 100403

Contents lists available at ScienceDirect

Open Ceramics

journal homepage: www.sciencedirect.com/journal/open-ceramics

Hybrid ceramic insulation made of oxide fiber ceramic matrix composite and paper-based ceramic for hot forming tools

Elmar Galiev [a,*], Ricardo Trân [a], Sven Winter [a], Felix Lindner [b], Georg Puchas [b], Cornell Wüstner [c], Mandy Thomas [c], Stefan Knohl [c], Verena Psyk [a], Stefan Schafföner [b], Walter Krenkel [b], Verena Kräusel [a]

[a] *Fraunhofer Institute for Machine Tools and Forming Technology, Reichenhainer Straße 88, 09126, Chemnitz, Germany*
[b] *Chair of Ceramic Materials Engineering, University of Bayreuth, Prof.-Rüdiger-Bormann-Str. 1, 95447, Bayreuth, Germany*
[c] *Papiertechnische Stiftung PTS, Pirnaer Str. 37, 01809, Heidenau, Germany*

ARTICLE INFO

Handling Editor: Dr P Colombo

Keywords:
FEM-Simulation
Tool insulation
Hot forming
Oxide fiber composites

ABSTRACT

Many modern automotive and aerospace components are heat-formed at temperatures up to 900 °C. Due to the high tool temperature, insulations are employed to reduce the heat loss and the energy consumption of the process. However, current insulation materials for the force flow of these processes still require active counter-cooling. In this study, the performance of a novel hybrid structure with improved insulation capability for such applications was investigated. It consisted of an outer frame made of an oxide fiber composite (OFC) and a paper-based ceramic (PBC) as a filler. The mechanical and thermal properties for both materials were determined and implemented in a finite element model (FEM) to numerically design the layout of a hybrid structure. Experimental load tests in process-oriented conditions validated the simulation results. The hybrid insulation appears promising, as mechanical stability and good insulation capabilities were confirmed.

1. Introduction

Components made by hot forming processes are playing an increasingly important role in automotive and aerospace industries, e.g. for titanium alloys [1]. For many titanium [2] and aluminum alloys [3] they offer advantages in terms of formability, as forming takes place above the recrystallization temperature of the metal. Depending on the material, the die temperatures for hot forming of sheets and tubes can reach up to 900 °C [4–7]. Due to the high tool temperature, the need for appropriate insulation to reduce heat losses and thus to increase energy efficiency is evident. The main purpose of the insulation in such high-temperature processes is energy and therefore cost saving through the use of smaller heating elements as well as easier and faster heating of the tools [8,9]. Another important advantage is the increase in service life and accuracy by avoiding impermissible heating of press components and tool guides [10], which otherwise must be prevented by counter-cooling systems between the tool and the press.

Thermal insulations for hot forming processes are divided into mechanically non-loaded (Fig. 1a) and loaded concepts (Fig. 1b). The latter are integrated into the force flow of the press and must therefore not only show good thermal insulation properties, but also exhibit mechanical stability to withstand the clamping force during the forming process. Conventional non-loaded insulation materials include ceramic fiber mats and mica-based materials, as well as glass fabric and vacuum-formed parts with a very low thermal conductivity of <0.1 W/mK. Table 1 summarizes some important properties of insulation materials. Due to their low compressive strength or temperature resistance, these materials are not suitable for the application in the force flow without further structural decoupling e.g. by implementation of an additional steel frame to counteract the resulting stress.

In the specific application area of the insulation used, particularly for hot forming tools in the power application area, the dimensions of the parts can vary from small parts of about 70 mm, for example in the superplastic hot tube gas forming process of titanium (Ti–3Al-2.5 V) [3], to large parts of 300 mm and more in hot stamping of aircraft parts [11].

In practice, special steels with relatively low thermal conductivity (e.g. GTCS-550, $\lambda = 7.5$ W/mK at room temperature) are often used if load-resistant insulating materials are required [14]. However, as their conductivity is still significantly higher than that of actual insulation materials, the associated heat loss makes it considerably more difficult to

* Corresponding author.
E-mail addresses: elmar.galiev@iwu.fraunhofer.de (E. Galiev), Felix.Lindner@uni-bayreuth.de (F. Lindner), Cornell.Wuestner@ptspaper.de (C. Wüstner).

https://doi.org/10.1016/j.oceram.2023.100403
Received 11 January 2023; Received in revised form 16 June 2023; Accepted 30 June 2023
Available online 14 July 2023

reach the desired tool temperature. Accompanied with their softening at higher temperatures, the application potential of steels is limited. The same applies to mica paper-based materials, which exhibit low thermal conductivity, but do not have a sufficient temperature stability.

A promising alternative to these materials may be provided by oxide fiber composites (OFC), as their thermal conductivity coefficient can exhibit values < 2 W/mK in the temperature range from room temperature to 1000 °C [15,16], depending on the used materials and the porosity. OFC are ceramic materials with quasi-ductile fracture behavior, i.e. improved damage tolerance, due to the incorporation of ceramic fibers in a ceramic matrix. They can be applied at temperatures in the range of up to 1000 °C [17–19], depending on the fiber used, and have a sufficiently high compressive strength (see Table 1). However, the material costs for OFC are significantly higher compared to steels and other conventional insulation materials [20], so that a novel, cost-effective approach is necessary to justify their use.

As the thermal conductivity coefficient varies largely between different ceramics, ranging from 2 W/mK for aluminum titanate to 140 W/mK for silicon-infiltrated silicon carbide [21], the material must be selected based on the specific application requirements. For the thermal insulation application considered in this work, an oxide material with low thermal conductivity is favorable, as it shows the required high-temperature stability in oxidizing environment. Additionally, the thermal conductivity decreases with a higher porosity which is, however, detrimental to the mechanical properties.

According to these considerations, a novel material denoted as paper-based ceramic (PBC), fabricated by sintering ceramic-filled special papers, was investigated as a thermally insulating filler component for the hybrid insulation as part of a feasibility study. This new kind of special ceramic [22–24] was optimized regarding its thermal insulation properties during this work. It can be produced in a cost-effective and simple paper-making process, in which ceramic powders, cellulose fibers and paper additives were combined to form so-called green compacts. During the final sintering step, the cellulose-based fibers are burned, leading to a material with defined high porosity and hence low thermal conductivity. In comparison to conventional insulation materials, no initial shrinkage and evaporation of degradation products will occur for application temperatures below the sintering temperature (1450 °C for the PBC in this work).

The aim of this paper was to develop a new type of insulation that combines high mechanical load resistance and excellent thermal insulating properties for the application in sheet metal forming processes. To meet those requirements, the concept of a hybrid structure comprising OFC and PBC was evaluated. Due to its low thermal conductivity, the novel PBC was tailored for its use as a filler material to increase the thermal insulation properties, while the OFC acted as the structural component to bear the compression load accompanied with the application in the force flow. To prevent the brittle PBC from damage, it was completely decoupled from the compression load. As the material costs for OFC in contrast to the PBC are significantly higher, the developed hybrid offers a more cost-effective and efficient solution than the OFC alone. Hence, a new material concept for thermal insulations with high mechanical loading was investigated, promising high energy saving potential.

Table 1
Specific characteristic values for insulation materials.

Property	Conventional insulation materials for setups without mechanical loading (e.g. ceramic fiber plate)	Conventional insulation materials for setups with mechanical loading (e.g. silicone resin impregnated mica paper)	Alternative insulation for setups with mechanical loading (e.g. oxide fiber composites)
Thermal conductivity [W/mK]	0.08 [12]	0.28 (at 200 °C) [12]	1.63 (at 900 °C) [13]
Continuous application temperature [°C]	max. 1100 [12]	max. 700 [12]	max. 1000 [13]
compression strength [MPa]	1.5 [12]	240 (at 250 °C) [12]	62 (at room temperature) [13]

2. Materials and methods

2.1. Oxide fiber composites

The OFCs were manufactured using a process based on pre-impregnated fibers (prepregs) [25–29]. Compared to a recently published study by Li et al. [30] this fabrication route does not require repeated reinfiltration steps and ceramic precursors, leading to OFC with higher matrix porosity. Additionally, it is not relying on autoclave technique and multiple high temperature cycles, hence letting the fabrication process in this work be considered simpler and straight forward. The OFC system for the hybrid comprised Nextel™720 fabrics (EF-19; 3 M Corporation, USA) and a mullite-based matrix. Prior to infiltration, the fabrics were desized for 2 h at 700 °C in air. The desized fabrics were infiltrated with a slurry containing 32 wt% glycerol relative to the solid content. The glycerol enabled the defined adjustment of the water content during a conditioning step in a climatic chamber (305SB/+10 JU, Weiss, Germany) at 25 °C and 47 %RH, and therefore ensured sufficient tack of the prepregs. The prepregs were laminated using a cold roll laminator, dried in a drying cabinet (FDL115, Binder,

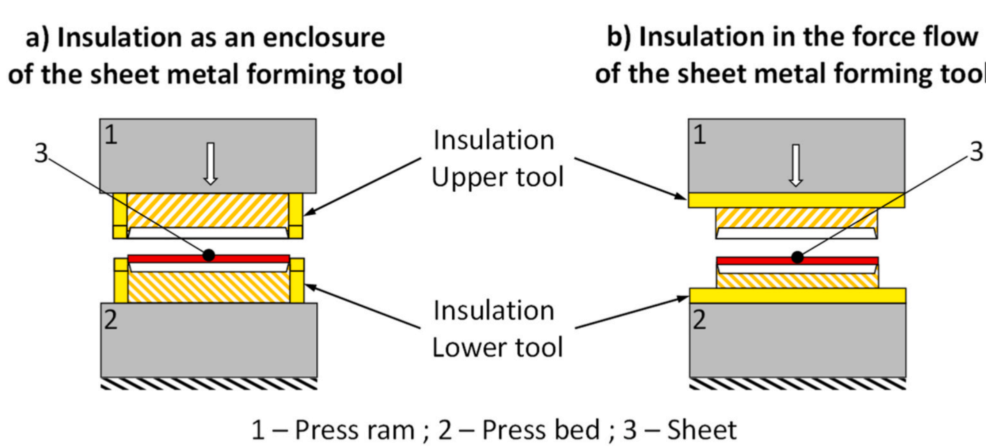

Fig. 1. Setup of a heated work tool using mechanically non-loaded a) and loaded b) insulation.

Germany) and finally sintered for 2 h at 1275 °C in air in a sintering oven (LH 60/14, Nabertherm, Germany).

For the application desired in this work, the usage of mullite as fiber and matrix material was deemed preferable to the mechanically more stable alumina (Al_2O_3), as its thermal conductivity of 6 W/mK at room temperature (3.5 W/mK at 1000 °C) [31] is far lower than the one of Al_2O_3, which is 33 W/mK at room temperature (7 W/mK at 1000 °C) [32]. Hence, the solid content of the slurry comprised 90 wt% mullite powder (Symulox M672, Nabaltec, Germany) and 10 wt% alumina powder (Taimicron TM-DAR, Taimei Chemicals Co., Japan). Besides the already mentioned glycerol, the liquid phase contained deionized water and a dispersing agent.

As prepregs with the combination of Nextel™720-fabrics and mullite containing slurries were not previously fabricated by the process described above, the parameters for the slurry composition and the processing conditions had to be tailored. The processing behavior of the slurry was investigated with a rheometer (MCR702 MultiDrive, Anton Paar, Austria) to evaluate the influence of the slurry components including glycerol and dispersant content on the slurry flow behavior in the prepreg state, i.e. after conditioning. The matrix morphology was analyzed by scanning electron microscopy (SEM; Sigma 300 VP, Zeiss, Germany).

2.2. Paper based ceramic

The PBC was developed in several research projects since 2003 [22–24]. By increasing the content of functional fillers, large quantities of flat, functional materials can be produced cost-effectively via established paper processing methods on a pilot paper machine (PAMA paper machinery GmbH, working width: 0,42 m). The preceramic paper was produced with a grammage of about 500 g/m^2, a ceramic filler content of 80 wt% and a corresponding cellulose fiber content of 20 wt% plus a small amount of paper additives, i.e. retention agent (0.1 wt%), binder (1.5 wt%) and starch (0.5 wt%). The obtained green body exhibited sufficient mechanical strength (width-related fracture strength of 3.5 kN/m in machine direction) which is vital for its handling in the following processing steps. Before the final sintering at 1450 °C, a debindering step between 200 °C and 500 °C was implemented, which was necessary to carefully remove all organic components from the green body. In order to create 3D structures, 45 to 50 single layers were stacked and sintered with a load (see Fig. 2 left). The resulting 3D PBC bodies (see Fig. 2 right) with a single layer thickness of 280 ± 20 μm exhibited satisfying cohesion, that allowed handling and further processing without delamination. Such bodies will henceforth be denoted as “inlays”, if they were designated to be inserted in the cavities of the hybrid structure. In general, it is possible to convert the semi-finished paper products into application-relevant, sometimes multi-layered or 3-dimensional structures, e.g. honeycomb plates with quadrangular or hexagonal structures.

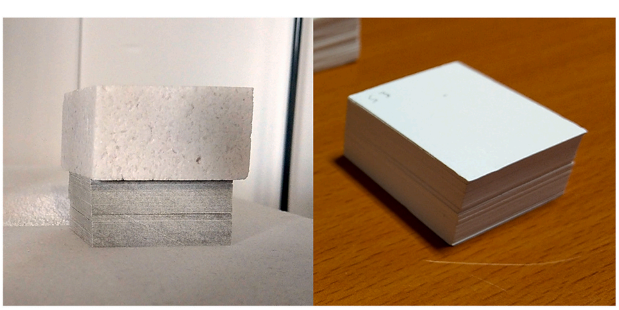

Fig. 2. Stack of highly filled paper (green body) under load before sintering (left), 3D PBC body (34 × 39 × 17 mm^3) after sintering (right) with a single layer thickness of 280 ± 20 μm. (For interpretation of the references to color in this figure legend, the reader is referred to the Web version of this article.)

For the PBC, the filler was a ceramic powder mixture which was tailored to the requirements of this work and finally consisted of 75 wt% alumina (Alumina CT3000 SG, Almatis GmbH, Germany; Taimicron TM-DAR, Taimei Chemicals Co., Japan) and 25 wt% zirconia (ZrO_2) (TZ-3YS-E, Tosoh Corporation, Japan). With the thermal conductivities of Al_2O_3 and ZrO_2 being 7 W/mK [32] and 2–3 W/mK [33] (both at 1000 °C), respectively, the low thermal conductivity values for the PBC originated mainly from the high porosity.

2.3. Method for development of hybrid insulations

In order to develop an optimized hybrid insulation, the properties of the individual component materials, i.e. OFC and PBC, were characterized in detail. Since the OFC was designated for the load-bearing frame structure of the hybrid insulation, its behavior under cyclic compression loading was investigated with a universal testing machine at room temperature (Z1485, Zwick Roell, Germany) as well as at 900 °C (RMC-mP 100, selfmade, Materials Testing Institute, University of Stuttgart) to simulate the opening and closing of the press. For the tests, a maximum load value of 100 MPa was defined, which exceeds the requirements for some of the targeted industrial applications.

Although the mechanical strength of the OFC is the key property for the hybrid insulation, it also contributes to the thermal insulation performance. Therefore, thermal properties were characterized for both OFC and PBC with the laser flash method, using the flash equipment LFA 467 HT HyperFlash in the case of OFC and LFA 427 in the case of PBC (both Netzsch, Germany) from room temperature to 1000 °C. Sample dimensions were 10 × 10xthickness mm^3, with the thickness being in the range of 400–600 μm for the PBC and 2–2.5 mm for the OFC. By heating the specimen front with a xenon flash lamp and measuring the resulting temperature rise on the back side with an infrared detector (InSb), the thermal diffusivity α was determined. The thermal conductivity was then calculated by Eq. (1), with the thermal diffusivity α, density ρ and specific heat capacity c_p.

$$\lambda = \alpha \times \rho \times c_p \quad (1)$$

Based on the thermal and mechanical properties of the investigated materials, a material model was created and implemented in FEM in order to design the hybrid insulation, including the determination of the minimum necessary thickness that sufficiently reduces heat flow from the hot forming tool to the press. The analysis was performed with an explicit thermal and mechanical solver in the commercial LS-DYNA software. The simulations of the temperature distribution were carried out with fully integrated solid elements (ELFORM 2) with edge lengths of 1 × 1x1 mm^3 and LS-DYNA R12.0.0. A standard MAT_24 was chosen as a plastic material model, in combination with MAT_THERMAL to describe the temperature component. The created model consisted of a heating layer representing the surface of the hot tool, a cooling layer representing the surface of the press bed and the investigated insulation in-between these two layers. The contact between the parts of the model was defined using “CONTACT_MORTAR_THERMAL”.

To enable a first experimental verification of the thermal values obtained by the LFA measurements and to validate and adjust the material model, samples consisting solely of OFC (all-OFC) and PBC (all-PBC) with an overall length of 100 mm, an overall width of 60 mm and a thickness of 20 mm were tested. While the length and width were given by the testing tool, the thickness was simulated based on boundary conditions for the temperature at the heated (900 °C) and cooled (21 °C) side of the insulation (see section 3.4). As the experimental determination of the temperature distribution required insertion of thermocouples in the insulation body, three holes with a diameter of 0.5 mm were modelled at different heights to increase the accuracy of the simulation (see Fig. 3a). The temperatures at the boundary between the heating and cooling plates and the sample were also monitored by thermocouples.

After a successful first validation of the simulation by comparing the results with the ones obtained from an experimental load test (as

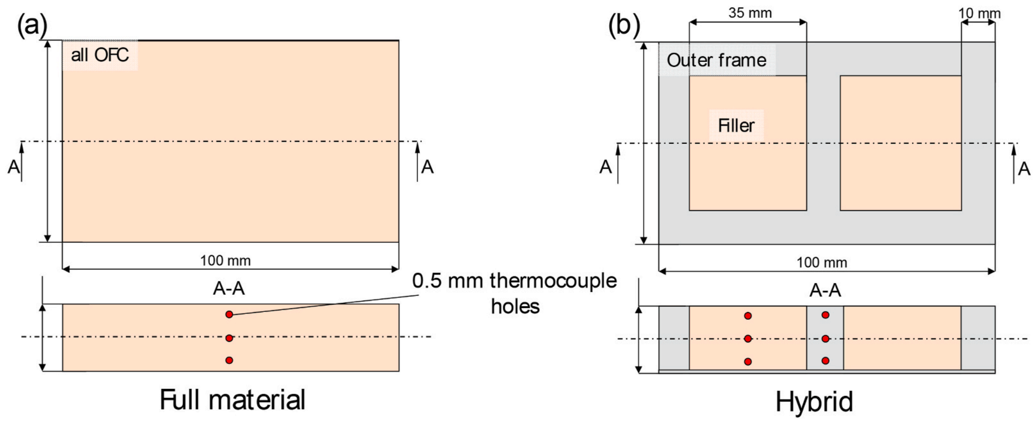

Fig. 3. All-OFC/All-PBC (a) and hybrid (b) sample geometry with measuring points for thermocouples indicated with red dots. (For interpretation of the references to color in this figure legend, the reader is referred to the Web version of this article.)

described in section 3.5.2), the model was adapted for the dimensioning of the hybrid component. Fig. 3b shows the considered geometry with an overall length of 100 mm, an overall width of 60 mm, a frame width of 10 mm and two filler cavities of 35 × 40 mm^2. Even though the simulation would have suggested a significantly higher PBC content, the design of a two-cavity frame was pre-defined by the authors to demonstrate the feasibility of non-trivial geometries and a minimum frame width of 10 mm was also set due to fabricational restrictions. Similar to the all-OFC and all-PBC samples, holes for thermocouples were considered in the hybrid as well. In this case, three holes for sensors were provided at different heights in each of the two base materials (Fig. 3b).

To validate the simulation experiments for the hybrid structure, experimental load tests were performed. According to the all-OFC and all-PBC samples, a test tool consisting of a heated and a cooled plate was used, between which the respective sample was placed (Fig. 4). Four ceramic heating elements with maximum surface powers of 150 W/cm^2 were implemented in the heated plate. The cooling plate was continuously cooled with water so that the temperature did not exceed 27 °C. To reduce the heat loss over the outer sample areas, an insulation shell was installed around the sample (not shown in Fig. 4), which was in close vicinity to the sample but not mechanically loaded.

The insulation specimen was placed on the preheated heating plate and the upper cooling plate was lowered until it was in contact with the top side of the specimen. Even though the target heating temperature was 900 °C, the real temperature at the surface of the heating plate ranged only between 870 °C and 890 °C due to heat losses and reaching the power potential of the heating elements. As will be seen, this temperature deviation can be deemed non-critical for assessing the overall application potential for the materials and the hybrid, respectively. A force of 60 kN was applied to the surface of the insulation component by the gas pressure springs shown in Fig. 4. The duration of the test was set to 1200 s, as the simulation predicted constant temperatures after this time, and the temperature was measured with K-type thermocouples, contacting the heating and cooling plate as well as the specimen. It must be pointed out that the thickness of the samples was not uniform due to fabrication-related variations in the layer thickness of the OFC frames (see Table 2).

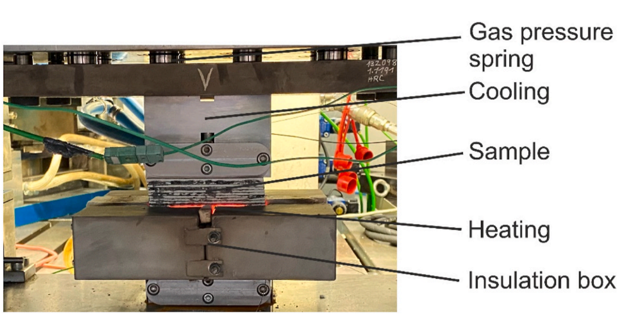

Fig. 4. Heated test tool.

3. Results and discussion

3.1. OFC optimization

Rheological measurements revealed major differences in the flow behavior of the slurry in the prepreg state after altering its composition from an alumina-zirconia powder system used hitherto [34,35] to the mullite system aspired in this work (Fig. 5). The distinct dilatancy at shear rates >10 1/s combined with the low viscosity level below this shear rate proved to have a negative impact on the processing behavior of the prepregs, as it was not possible to squeeze out excess slurry from the prepreg plies, leading to low fiber volume contents in the composites. After examining the impact of glycerol and dispersant content as well as the conditioning humidity on the rheological properties of the slurry, an optimized slurry composition was defined, which also comprised a mullite-alumina powder composition instead of pure mullite. This alternated the flow behavior (Fig. 5) and led to better processability and therefore a higher fiber volume content of the OFC produced with this slurry (Fig. 6 right).

For the different powder combinations (pure mullite, 90/10 wt% mullite/alumina) investigated, a high matrix densification was detected, which resulted in matrix crack formation (segmentation cracks) due to the constrained sintering applied on the matrix by the non-shrinking fiber network (Fig. 6 a-b). This high level of sintering was attributed to the sintering activity of the powders used and did not show significant change with variations of the powder types and fractions used in this work. In general, both images show rather comparable microstructure, with unfavorable matrix-free areas within the fiber bundle (Fig. 6 c-d) that might be traced back to the lower viscosity level of the mullite containing slurries after conditioning. Even though a higher level of sintering of the matrix in OFC reduces the damage tolerant behavior, it

Table 2
Experimental matrix of the samples tested in the hot press.

Sample	Sample thickness in mm	Number of slots for thermocouples	Test duration in s
All-OFC	24	3	1200
All-PBC	20	3	
Hybrid (OFC and PBC)	24	6	

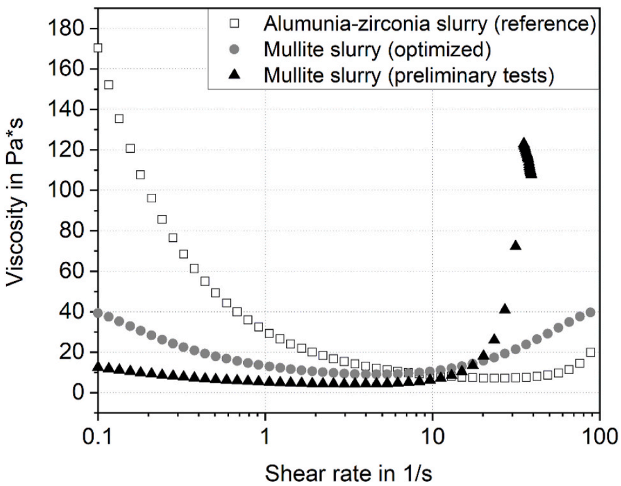

Fig. 5. Viscosity curves of mullite slurries before and after optimization in comparison to an alumina-zirconia slurry (all slurries were measured in the prepreg state, i.e. after conditioning).

also increases the off-axis-properties and the compression strength [36], which is of major interest for the application under compressive load as investigated in this paper.

3.2. PBC characterization

As already described in section 2.2, 3D PBC bodies consisting of Al_2O_3 and ZrO_2 were obtained by sintering highly filled papers in a stack under compression load. Fig. 7 shows SEM micrographs of the microstructure from both the green body (left) and the resulting PBC (right).

The green body (Fig. 7 left) shows a mixture of cellulose fibers, which are visible as darker, predominantly ovally shaped cross sections, together with the Al_2O_3 and ZrO_2 filler powder (brighter areas). The SEM image of the highly porous PBC displays the porous ceramic matrix in bright color, whereas the pores are filled with an organic resin and therefore appear in dark grey. It can be seen that the pores are evenly distributed over the whole cross section of the material.

The PBC was further characterized by mercury porosimetry, which yielded values for the open porosity of 50.3% and an average pore diameter of 10.8 μm. Analysis of the thermal conductivity revealed values of 0.77 W/mK at room temperature, which dropped to 0.42 W/mK at 1000 °C. By the double ring method (derived from DIN 51105) a

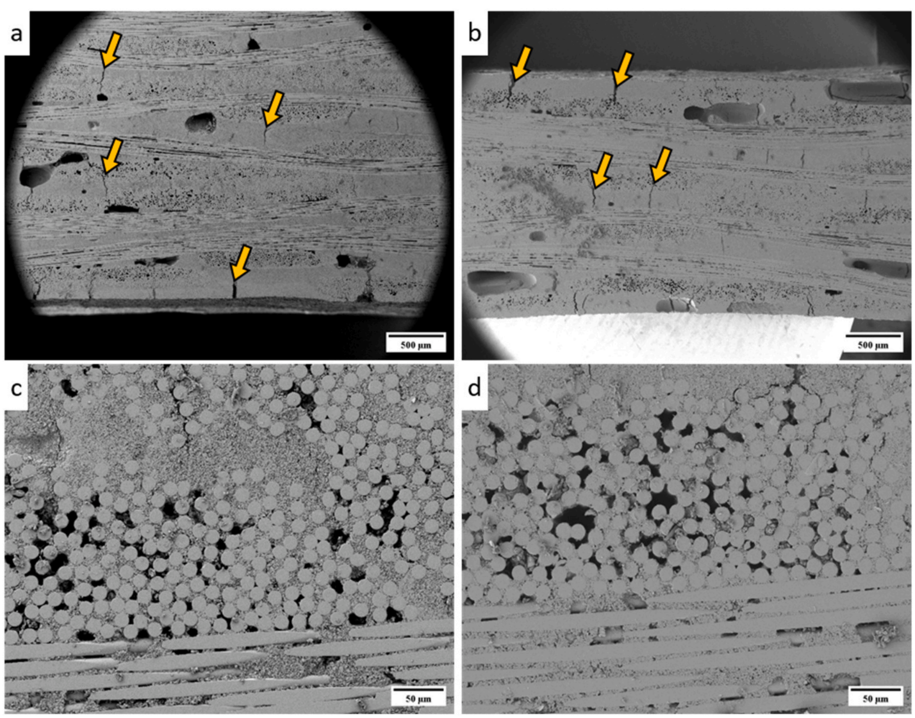

Fig. 6. Microstructure of OFCs with matrix compositions mullite/mullite (a, c) and mullite/alumina (b, d) obtained by SEM. top: shrinkage induced matrix cracks perpendicular to the fiber directions (marked with an arrow). Bottom: matrix-free areas within the fiber bundle.

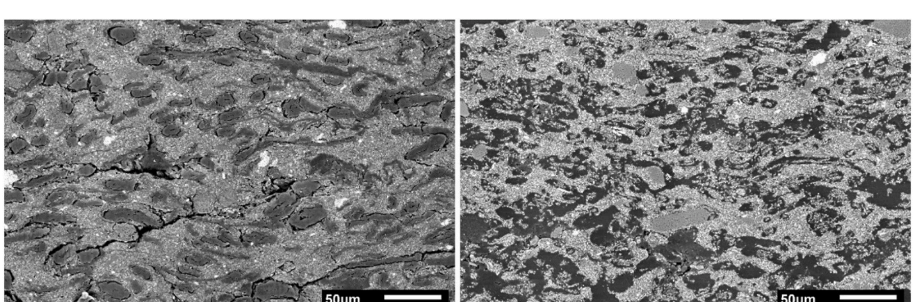

Fig. 7. Microstructures of the highly filled paper green body (left) and the sintered PBC (right).

bending strength of 20.2 MPa was measured, which was enough for safe handling and insertion into the OFC frame during the manufacturing process of the hybrid insulation.

3.3. OFC characterization

3.3.1. Characterization of mechanical properties

Since the OFC frame in the hybrid structure served to absorb the clamping force of the press, tests were conducted to determine the mechanical properties of this material in through-thickness direction (i.e. perpendicular to the fibers) under compression loading. Fig. 8 shows the test setup of the cyclic load tests performed on the OFC and illustrates the results by plotting the compressive stress measured during the tests over the sample compression for selected load cycles. The loading was performed with a deformation speed of 2 mm/min without a defined load frequency and included full removal of the force at the end of each load cycle. Due to the long testing time, the number of specimens was narrowed down to a maximum of two. The OFC sample in Fig. 8 (10 × 10 × 6 mm^3) was fabricated with an all-mullite slurry and was sintered at 1225 °C.

Surprisingly, the sample showed significantly more deformation during the first load cycle compared to the following cycles. Furthermore, it featured several discontinuities that were not present in the other graphs. Instead, for all subsequent loads the curves were steeper, more continuous and mostly congruent. This observation was identified as a settling effect, which means that the sample is mechanically damaged and therefore shows a certain degree of non-elastic deformation (settling) after the first loading. This can be attributed to the non-uniform thickness (average value 6.19 mm) of the sample, which led to an overload in the elevated areas of the sample with associated failure of individual matrix areas. Additionally, the breakup of weak sintering bridges between particles or between particles and fibers was also expected to take place throughout the full sample volume during the initial load cycle. However, the high reproducibility of the curves recorded after the first load cycle suggests that this was exclusively the case for the initial loading.

Up to the maximum number of 200 load cycles considered here, the sample was able to carry the applied load without showing any indications of failure. The same tests, yet at the targeted application temperature of 900 °C, confirmed the results obtained at room temperature. Due to the high-temperature condition experimental setup, the number of load cycles was limited to 100 and a minimal force equivalent to 10 MPa remained on the sample at the end of each cycle. Loading and unloading was force-controlled with 320 N/s. For comparison, commercially available OFC from two different suppliers (OFC C1, OFC C2, Table 3) were tested similarly and revealed the same stability for cyclic compression loading, with minor deviations in the deformation behavior (Fig. 9). Note that for easier comparison between the samples the absolute deformation was depicted. With this display, the permanent settling of the sample can be observed by a shift of the starting points for each load cycle towards higher deformation. While the curves for load cycle 50 and 100 for the OFC developed in this work (denoted as OFC) and OFC C1 were very similar, the curves obtained for OFC C2 showed a continuous drift towards higher compression values. This indicates that damaging of the microstructure was persistent for OFC C2 throughout the loading processes and a failure of the component with increasing load cycles can be expected. As the other two OFC did not show this drift, their stability can be deemed superior to OFC C2.

3.3.2. Characterization of thermal properties

Fig. 10 shows the thermal conductivity of the OFC (through-thickness direction) and the PBC as a function of temperature. As expected, the value of the PBC was lower than that of the OFC, while the values decreased with increasing temperature for all samples. The comparison of the OFC revealed the lowest thermal conductivity (<1.3 W/mK) for the newly developed material (OFC). While OFC C2 exhibited only slightly higher values (<1.5 W/mK), the difference for OFC C1 was more pronounced especially in the lower temperature range. This can be attributed to the non-mullitic matrix and fibers used in OFC C1, while the deviation between OFC C2 and OFC, with rather comparable material compositions, can be accounted to the higher amount of open porosity in the latter. The open porosity of the OFC and the PBC was measured with Archimedes' method and is shown in Table 4.

3.4. Numerical dimensioning of the hybrid insulation

In a first step, the necessary thickness of the samples for the experimental tests was determined by simulation in LS-DYNA. The key criterion was the maximum temperature of the element layer adjacent to the cooling plate, which per definition should not exceed 100 °C to prevent the cooling liquid from boiling. As the dimensions of the finite elements was 1 mm^3, this represented the mean temperature at a distance of 0.5 mm from the cooling plate. The boundary temperature

Table 3
Information on the commercial OFC.

OFC type	Matrix	Fiber
OFC C1	Alumina-zirconia	Nextel™610
OFC C2	Mullite	Nextel™720

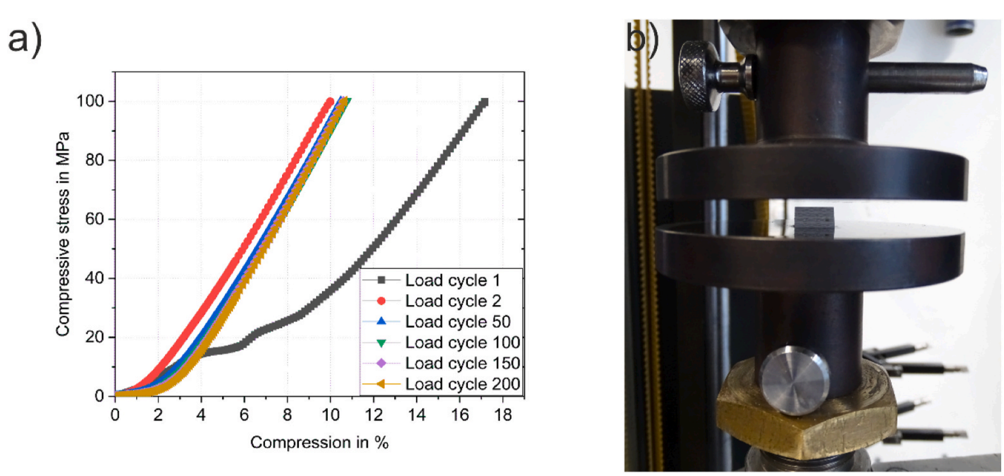

Fig. 8. Mechanical behavior of an OFC sample in a cyclic compression test (through-thickness direction) at room temperature with a maximum load of 100 MPa. a) Stress curves for selected load cycles; b) Specimen placed in the testing machine.

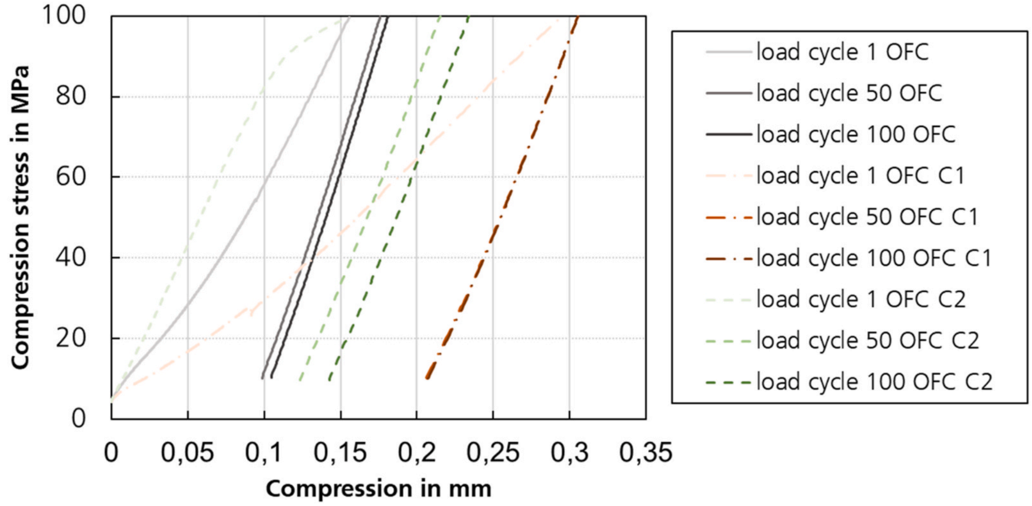

Fig. 9. Compression curves for selected load cycles of the OFC developed in this work (OFC) as well as two different commercial OFC materials (OFC C1, OFC C2) in a cyclic compression test (through-thickness direction) at 900 °C with a maximum load of 100 MPa.

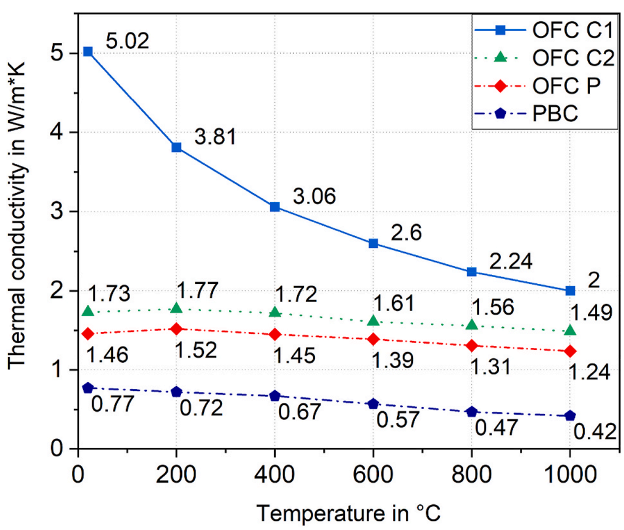

Fig. 10. Thermal conductivity of OFC (through-thickness direction) and PBC at different temperatures determined by means of the laser flash method.

Table 4
Density and open porosity of the OFC and the PBC.

	OFC	OFC C1	OFC C2	PBC
Density in g/cm^3	2.3	2.8	2.5	1.9
Open porosity in %	29.9	31.5	24.3	>50.3

conditions were defined as 900 °C at the tool and 21 °C at the cooling plate. Fig. 11 compares the simulated temperature distributions after 1000 s for all-OFC insulations of 10 mm (Figs. 11a) and 20 mm (Fig. 11b) thickness, respectively, as well as the hybrid insulation (20 mm). As expected, the temperature close to the cooling plate decreased with increasing insulation thickness. To ensure the aforementioned temperature criterion, a thickness in the range of 20 mm was necessary in case of the all-OFC. For the hybrid insulation (Fig. 11c) the temperature close to the cooling plate was significantly lower compared to the all-OFC sample with the same thickness of 20 mm. This confirmed that the PBC inserts significantly improved the insulation performance of the hybrid component. Based on these results, a thickness of 20 mm was selected for the samples fabricated for further experimental tests.

3.5. *Experimental implementation and validation*

3.5.1. *Manufacturing hybrid insulation samples*

The OFC frame was manufactured by the manual lay-up of prepreg strips to provide the cavities intended for the PBC-filler and in order to use as little OFC as possible to safe costs. To ensure their geometrically correct alignment, a 3D-printed template was used. This was designed with undersized cavities to allow post-processing to the final dimension after sintering of the composite by means of a diamond wire saw and abrasive paper. The average thickness of the OFC frames (four fabric layers) after sintering was approximately 2 mm with a fiber volume content of around 35% and with deviations of up to 0.18 mm over the entire frame (Fig. 12).

For the production of the hybrid insulation, nine to ten OFC frame layers, a lower OFC cover plate and the PBC inlays were stacked and joined using an inorganic adhesive (Ceramabind™ 642, Aremco, USA). Due to the already discussed settling and deformation behavior of the OFC, the height of the inlays had to be slightly below the upper edge of the frame structure to avoid contact with the press mold and thus mechanical damage during the application of the clamping force. The adhesive was cured in two stages (2 h at 95 °C, 4 h at 150 °C), followed by a heat treatment at 1000 °C (3 h) to prevent thermal changes in the adhesive layer during the tests. For the inline temperature measurement, notches were inserted in the corresponding frame layers by means of a diamond cutting disc and filled with a sacrificial phase. The sacrificial phase was covered with the adhesive in the subsequent joining step and thermally decomposed without residue during the heat treatment, creating a hole with a diameter of 0.5 mm for the thermocouples to be implemented. Due to the high strength of the ceramics studied and the small diameter of the holes required, the optimal size of the thermocouples used was chosen to minimize the distortion of the experimental data obtained. The thermocouples in the selected positions were necessary to validate the simulation results, and since the hybrid insulation has a more complex geometry than the monolithic one, more holes were used to measure the temperature inside the hybrid insulation as well as at the contact point between the two hybrid materials. The all-OFC sample was fabricated accordingly, while the all-PBC sample was produced by stacking and subsequent sintering of green body layers (see section 2.2). All specimens for the thermo-mechanical load tests and their positioning relative to the heated and cooled surfaces are shown in Fig. 13.

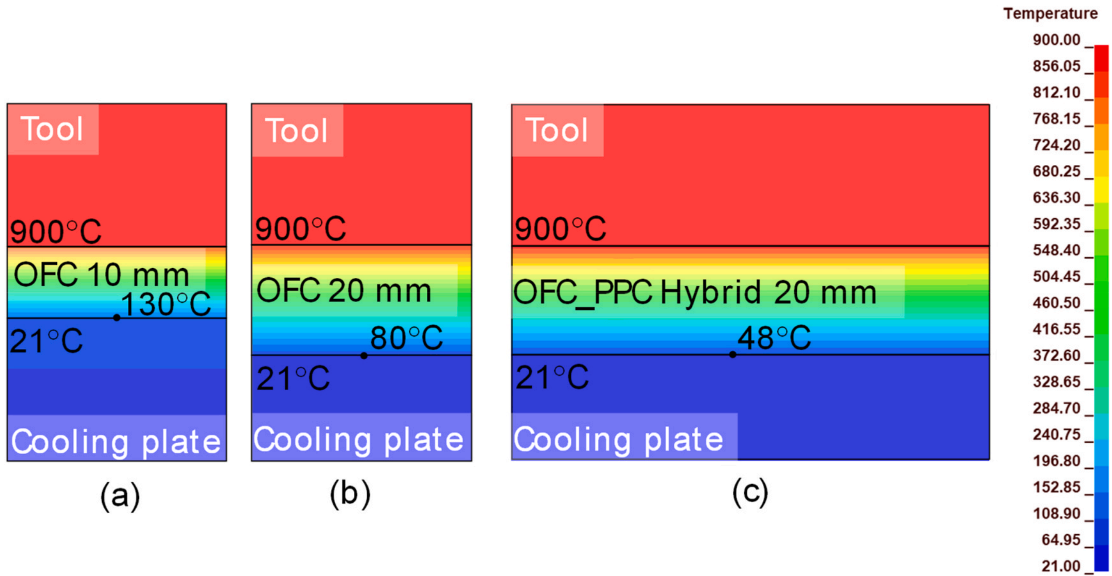

Fig. 11. Comparative analysis of the effect of the insulation thickness on the temperature distribution (a) OFC 10 mm exceeded the temperature limit of 100 °C near the cooling plate; (b) OFC 20 mm achieved the temperature requirement; (c) hybrid 20 mm yielded the highest temperature drop.

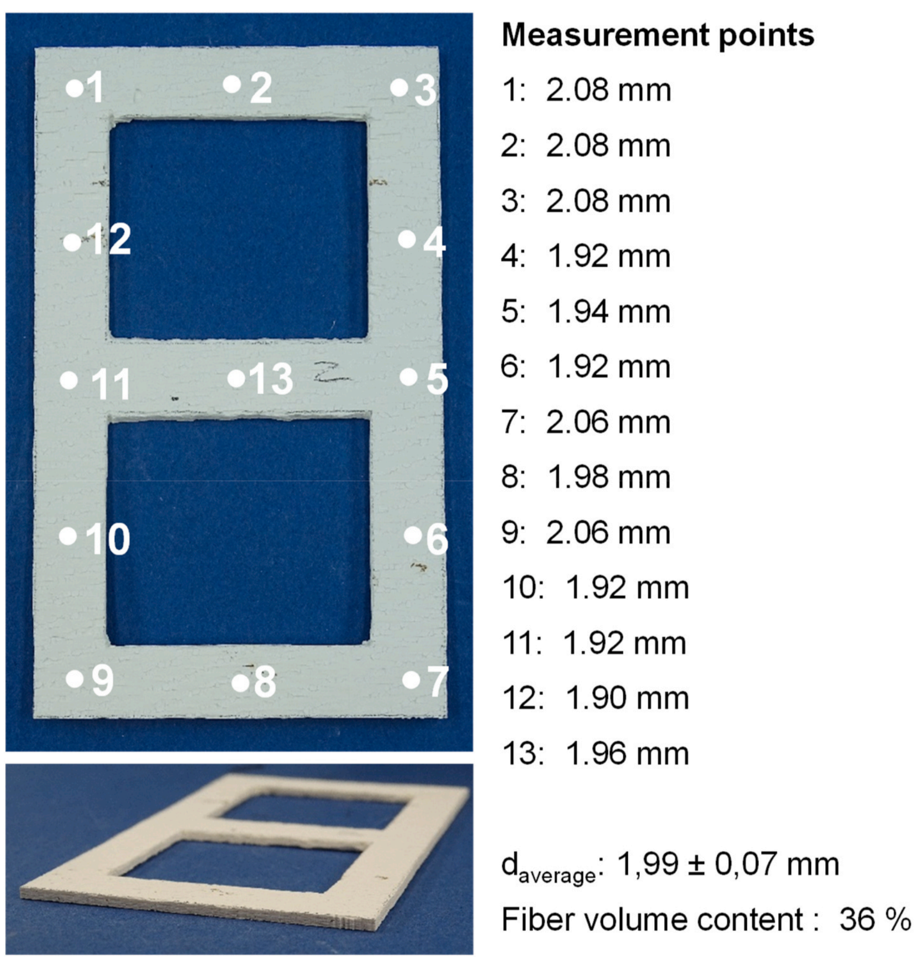

Fig. 12. Dimensional accuracy of an OFC frame.

3.5.2. *Comparison of experimentally and numerically determined temperature distributions*

The first samples for testing were the ones shown in Fig. 13a and b, corresponding to the all-OFC and all-PBC, the resulting hybrid geometry is shown in Fig. 13c. With these samples the thermal conductivity values determined earlier and the corresponding material model was verified.

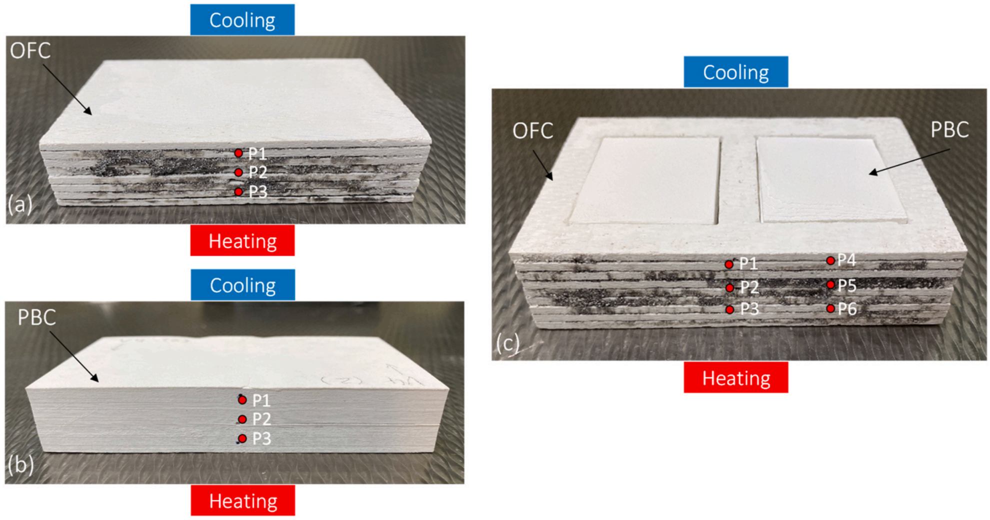

Fig. 13. a) All-OFC sample b) All-PBC sample c) hybrid sample.

Furthermore, it was possible to visualize respective insulating capacity. The measured temperature versus time curves at the different measurement points are shown in Figs. 14 and 15 in direct comparison to the corresponding numerical results for both OFC and PBC.

The temperature curves obtained from the experiments are shown as continuous lines. It can be seen that after about 1000 s, the curves flatten out and there is no further temperature change for both PBC and OFC. While the simulation data (dotted lines in Figs. 14 and 15) for OFC yielded deviations of 11 °C for P3 and 38 °C for P2, the simulation results for the PBC were more accurate, with a maximum deviation of 11 °C at P3. This was caused by the OFC sample consisting of multiple layers of OFC joined by adhesive layers between them (see 3.5.1), whereas in the simulation a homogeneous material was assumed. As the adhesive partially fills up the porosity and is expected to have a higher thermal conductivity itself, this led to a change of the thermal properties of the joined OFC compared to the non-joined samples tested by LFA, which is not covered in the simulation. Additionally, the PBC sample was not as highly compressed between both heating and cooling plate as the OFC, due to its lower mechanical strength. This might have led to a worse contact and hence lower heat transfer at the hot and cold side of the insulation. The data obtained from simulation are in line with the experimental results, which basically validated the material models for the numerical design and dimensioning of the tool and the insulation. Hence, their validity for the simulation of the full materials and therefore the hybrid structure was proven.

A more detailed examination of the experimental results displayed in the diagram for the all-OFC sample revealed the maximum difference between points P1 (near the cooling board) and P3 (near the heating plate) to be equal to 622 °C. For the PBC sample this difference was 638 °C and therefore only slightly higher than the all-OFC. As the thermal conductivity of the PBC was determined to be significantly lower than the OFC, this difference was expected to be more pronounced. However, the sample thickness of the PBC was only 20 mm in contrast to 24 mm for the all-OFC. Hence, the temperature gradient in the all-PBC sample was steeper, indicating a lower thermal conductivity of the PBC compared to the OFC. To mitigate this influence, a simulation was carried out to calculate the temperature gradient in an all-PBC sample of the same thickness as the all-OFC sample (24 mm). The results are shown in Fig. 16 and revealed an increased temperature gradient of 654 °C, which was 32 °C higher than for the all-OFC.

The test results for the hybrid insulation are shown in Figs. 17 and 18 and revealed considerable deviations between experimental and simulation results in the OFC and PBC sections of the hybrid. Yet, these differences are of the same magnitude as already obtained, especially for the all-OFC. Again, the largest difference was detected in the middle of the OFC section because the thermal properties in the material model did not consider the contribution of the adhesive layers. This simplified approach is also expected to be responsible for the different results for P6 in the PBC, as an adhesive layer as joint between OFC and PBC was present. Compared to the results for all-OFC and all-PBC, the temperatures at P3 and P6, respectively, were simulated and measured to be higher in the hybrid, which originates from the reduced distance between P3 and P6 from the heating plate, as the OFC cover plate was thinner. Also, the temperature at the surface of the heating plate was

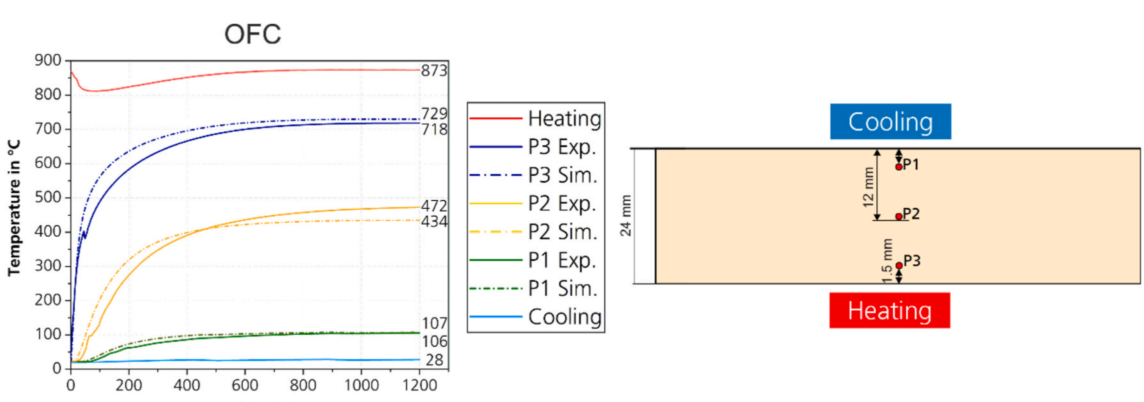

Fig. 14. Comparison of measured and numerically simulated temperature versus time curves for OFC.

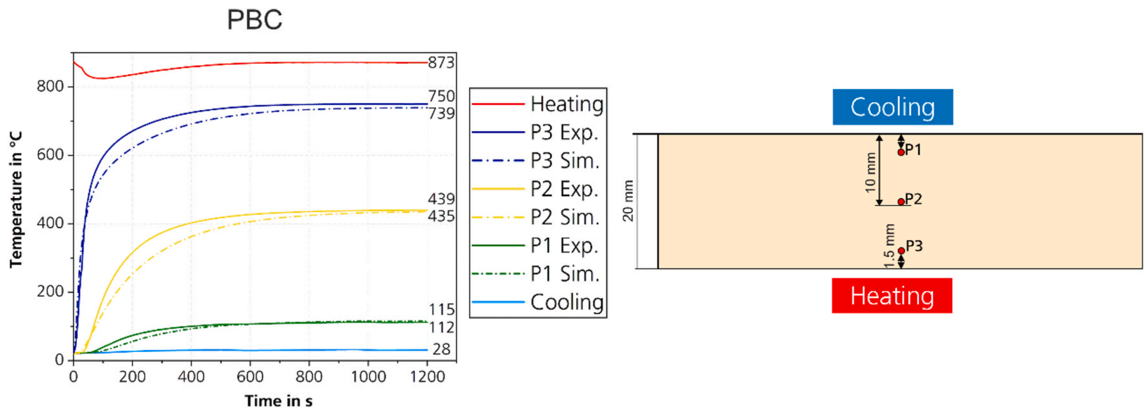

Fig. 15. Comparison of measured and numerically simulated temperature versus time curves for PBC.

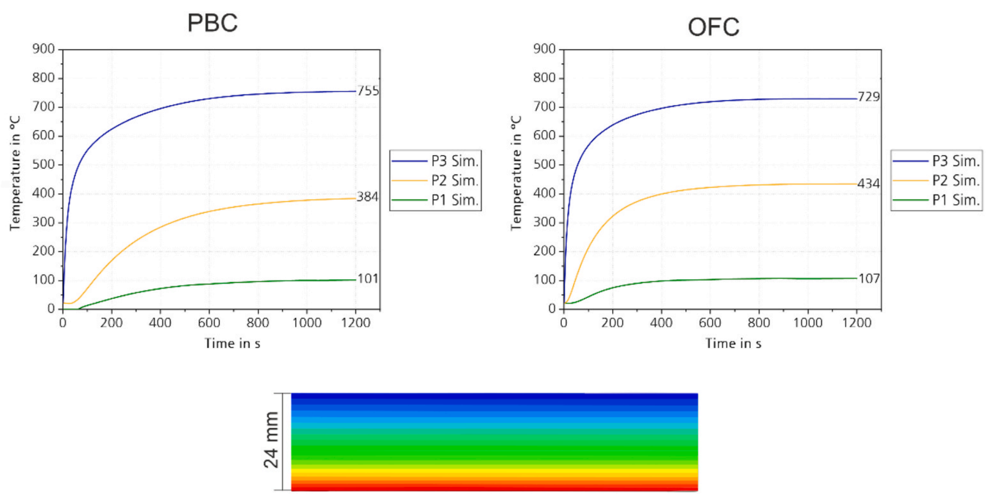

Fig. 16. Comparing the simulation results for 24 mm thick OFC and PBC monolithic samples.

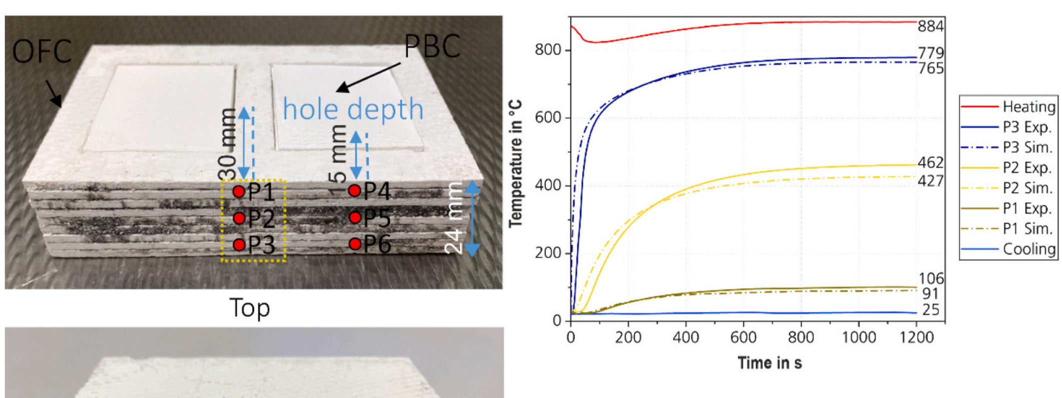

Temperature	Temperature at				
	Cooling	P1	P2	P3	Heating
Nummerically determined	25°C	107°C	434°C	729°C	884°C
Measured	25°C	106°C	472°C	718°C	884°C

Fig. 17. Comparison of experimental data and simulation results for hybrid insulation for points P1–P3.

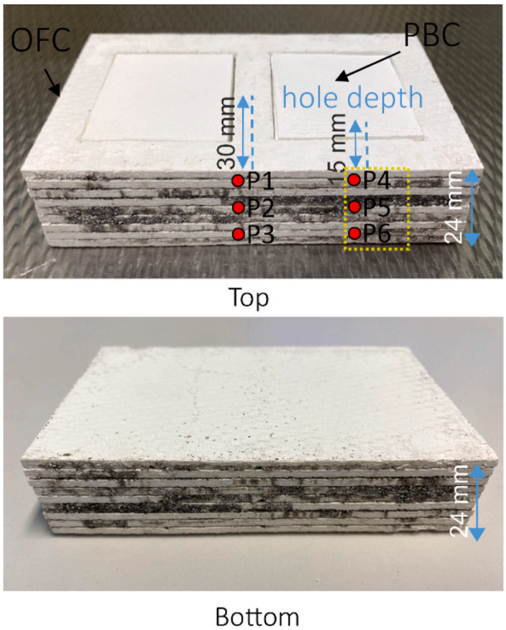

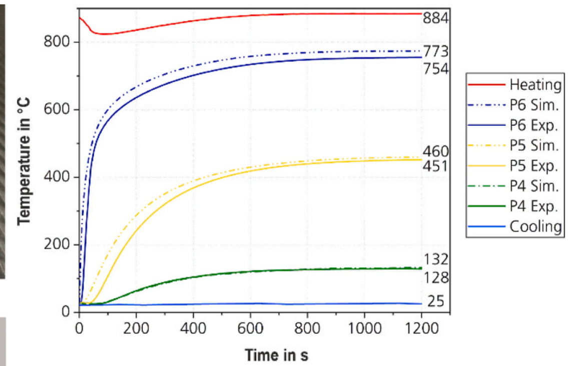

Temperature	Temperature at				
	Cooling	P4	P5	P6	Heating
Nummerically determined	25°C	132°C	460°C	773°C	884°C
Measured	25°C	128°C	451°C	754°C	884°C

Fig. 18. Comparison of experimental data and simulation results for hybrid insulation for points P4–P6.

11 °C higher.

Another striking observation was the difference of the temperature in P1 and P4. As the OFC yielded values of 91 °C and 106 °C for simulation and experiment, respectively, the PBC revealed 132 °C and 128 °C. This considerable temperature difference between OFC and PBC can be accounted to the mechanical decoupling of the PBC in the hybrid structure, which leaves a small gap between the PBC and the cooling plate to avoid mechanical failure due to compression force. However, this small gap adds a convectional term to the heat conduction resistance of the heat transfer, and thereby reduced the temperature drop off in the PBC. In contrast, the OFC frame is exposed to considerable load and therefore provides good contact for heat transport. As the fit of the simulation results was deemed sufficient in case of the all-OFC and all-PBC samples, the same can be stated here as well.

3.6. Hybrid design

Even though the rectangular frame structure design of the hybrid insulation investigated in this work has a number of advantages such as simplicity in manufacturing, simple post-processing and little OFC waste, different hybrid geometries are feasible. However, due to the higher material expense and the more sophisticated post-processing methods, e.g. waterjet cutting, the fabrication will become more costly once non-rectangular designs are chosen.

In general, the design of the hybrid insulation must be adjusted primarily to the mechanical loads that are applied during the press forming process to avoid mechanical failure during service. As the cyclic mechanical load resistance of the OFC is limited, the OFC fraction in the hybrid insulation must be related to the required clamping force, which can be accomplished by increasing the number of the frame bars or by broadening them. Fig. 19 details this relation as the resulting compression stress in the OFC over the area content of PBC in a hybrid structure with given external dimensions (60 × 100 mm), loaded with a clamping force of 60 kN. The example clearly shows a non-linear load increase in the OFC with increasing PBC content in the hybrid. By defining the maximum load level of the OFC, a ratio of OFC and PBC content can be determined, that ensures sufficient overall strength of the hybrid structure and simultaneously maximizes its insulation performance. For the OFC investigated in this work, a cyclic compression load resistance up to 100 MPa (through-thickness direction) was determined, which would theoretically allow the PBC content to be increased to approximately 85%. In practice, multiple detrimental effects on the mechanical integrity of the component need to be considered, such as lateral forces, stress peaks, material inhomogenities and the impact of the adhesive

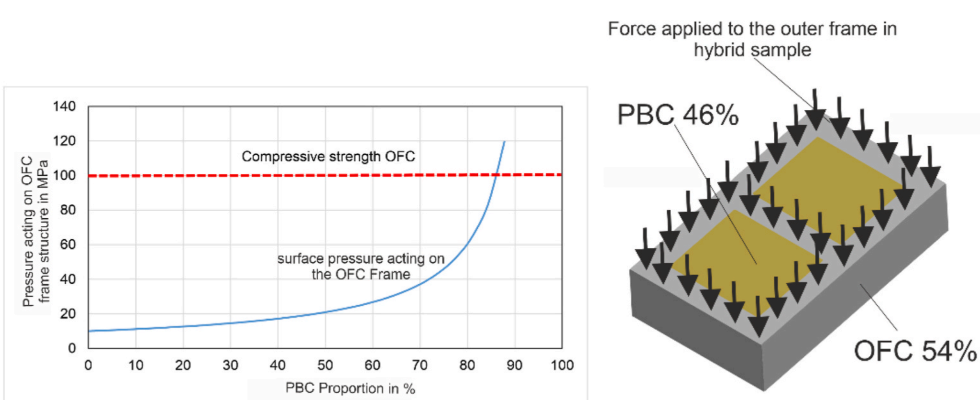

Fig. 19. Compression stress on the OFC frame in relation to the PBC content of the hybrid structure for a clamping force of 60 kN (left), hybrid structure of the experimental loading tests with respective proportions of OFC and PBC detailed (right).

layers. Hence, a higher OFC fraction is required. The proportion used in this work, i.e. 46 % PBC and 54% OFC, led to a rather low compression stress of <20 MPa in the OFC, hence the PBC fraction could be increased drastically. Yet, the small outer dimensions of the tool used in this study makes this task difficult, as the OFC frame bars must be narrowed down significantly, making their handling during the assembly process of the hybrid structure difficult. In this case, the usage of OFC in in-plane direction would be preferable, as their thickness, which in this case corresponds to the frame bar width, can easily be reduced to 1.4 mm and lower. An interlocking setup of upright frame bars can be envisioned, reducing the necessary amount of adhesive. The mechanical and thermal properties of the OFC vary between through-thickness and in-plane direction, i.e. the compressive strength is somewhat lower and the thermal conductivity is higher in in-plane direction, rendering this direction less favorable for the chosen application. However, by using the altered values for the simulation, this can be addressed by a different design of the hybrid structure.

4. Conclusions

The aim of this study was the development of a tool insulation for hot forming processes with improved mechanical and thermal characteristics for the use in the force flow at temperatures of up to 900 °C. For this purpose, a new type of hybrid insulation combining oxide fiber composites (OFC) and paper-based ceramics (PBC) was developed. In this concept the mechanical properties of OFC were exploited to absorb the compressive load during the forming process, while the excellent thermal insulation properties of the PBC enhanced the insulation performance and allowed reduced costs compared to a pure OFC insulation. The optimized materials exhibited characteristic values for porosity and thermal conductivity (at room temperature) of 29.9% and 1.46 W/mK for the OFC (through-thickness direction) as well as 50.9% and 0.77 W/mK for the PBC. As part of our research, we also compared the energy efficiency of our insulation against conventional materials. A GTCS 550 steel material with low thermal conductivity was used as the conventional insulation material. As part of the simulation to evaluate the energy efficiency of the considered insulations, the parameter "heat flow" was evaluated in LS DYNA for each of the considered insulation materials separately, as well as for the hybrid insulation (Fig. 20). The simulation showed, that in order to even remotely achieve the heat flow density of the hybrid insulation, the thickness of the steel insulation would have to be five times as high.

Numerical simulation clearly showed that the steel material insulates significantly worse than the ceramic hybrid insulation, both at the same thickness as the hybrid insulation and at 5 times the thickness. It can be concluded that the developed insulation is not only significantly more efficient, but also significantly more space saving, which is highly relevant for large forming dies. In an experimental test setup the enhanced insulation performance of the PBC was demonstrated, as the temperature at the cooled side of the insulation was 32 °C lower for the PBC. Based on specifications, a hybrid structure was developed and tested under mechanical and thermal load similar to industrial manufacturing conditions. Its stability and insulation capability was proven for temperatures of up to 870 °C and a clamping force of 60 kN. A good approximation of experimental and simulation results was achieved, which enables the design of optimized hybrid components for different hot forming applications, e.g. depending on the tool geometry and the clamping force necessary.

Author contributions statement

Elmar Galiev: Writing - Original Draft, Writing - Review & Editing, Conceptualization, Methodology, Validation, Formal analysis, Investigation, FE-Simulation; Ricardo Trân: Writing - Original Draft, Writing - Review & Editing, Conceptualization, Methodology, Investigation, Project administration; Sven Winter: Writing - Original Draft, Writing - Review & Editing; Felix Lindner: Writing - Original Draft, Writing - Review & Editing, Conceptualization, Methodology, Validation, Formal analysis, Investigation; Georg Puchas: Writing - Original Draft, Writing - Review & Editing, Conceptualization, Methodology, Validation, Formal analysis, Investigation, Project administration; Cornel Wüstner: Writing - Original Draft, Writing - Review & Editing, Project administration, Investigation; Mandy Thomas: Methodology, Validation; Stefan Knohl: Project administration, Conceptualization; Verena Psyk: Writing - Review & Editing, Conceptualization; Stefan Schafföner: Writing - Review & Editing, Supervision; Walter Krenkel: Writing - Review & Editing, Supervision, Funding acquisition; Verena Kräusel: Writing - Review & Editing, Supervision, Funding acquisition.

Funding

The "ForWerk" project (Nr. 20646BG) of the Papiertechnische

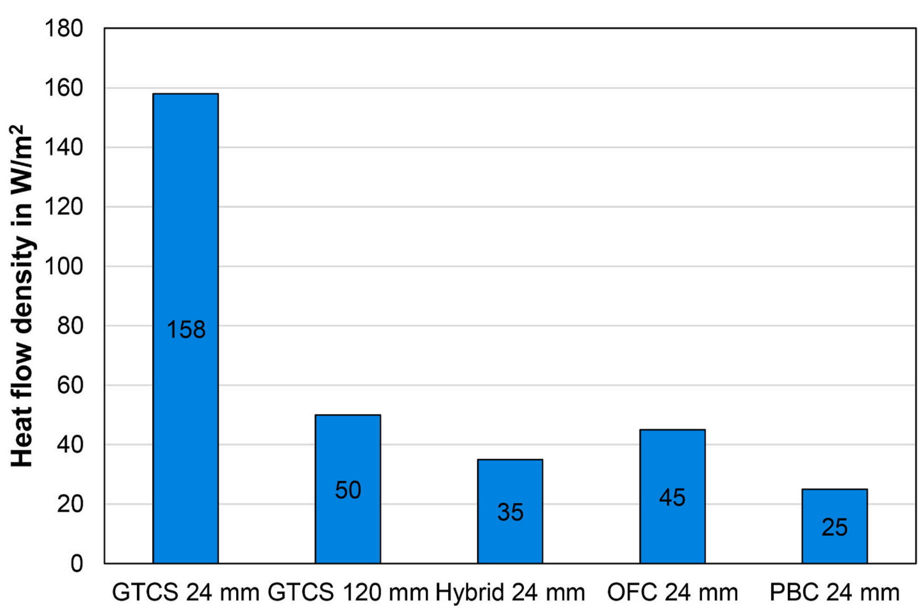

Fig. 20. Numerical analysis of heat flow for different types of insulation.

Stiftung (PTS), Pirnaer Straβe 37, 01809 Heidenau (Germany) was funded by the Federation of Industrial Research Associations (AiF) within the program for sponsorship by Industrial Joint Research (IGF) of the German Federal Ministry of Economic Affairs and Energy based on an enactment of the German Parliament.

Declaration of competing interest

The authors declare that they have no known competing financial interests or personal relationships that could have appeared to influence the work reported in this paper.

References

[1] K. Wang, C. Shi, S. Zhu, Y. Wang, J. Shi, G. Liu, Hot gas pressure forming of Ti-55 high temperature titanium alloy tubular component, Materials 13 (2020) 4636, https://doi.org/10.3390/ma13204636.
[2] P.K. Saha, Major aircraft materials and its classification, in: Aerosp. Manuf. Process., CRC Press, Boca Raton, 2016, https://doi.org/10.1201/9781315367965.
[3] R. Trân, F. Reuther, S. Winter, V. Psyk, Process development for a superplastic hot tube gas forming process of titanium (Ti-3Al-2.5V) hollow profiles, Metals 10 (2020) 1150, https://doi.org/10.3390/met10091150.
[4] D. Chantzis, X. Liu, D.J. Politis, O. El Fakir, T.Y. Chua, Z. Shi, L. Wang, Review on additive manufacturing of tooling for hot stamping, Int. J. Adv. Manuf. Technol. 109 (2020) 87–107, https://doi.org/10.1007/s00170-020-05622-1.
[5] S. Hafenstein, E. Werner, J. Wilzer, W. Theisen, S. Weber, C. Sunderkötter, M. Bachmann, Influence of temperature and tempering conditions on thermal conductivity of hot work tool steels for hot stamping applications, Steel Res. Int. 86 (2015) 1628–1635, https://doi.org/10.1002/srin.201400597.
[6] H. Liu, C. Lei, Z. Xing, Cooling system of hot stamping of quenchable steel BR1500HS: optimization and manufacturing methods, Int. J. Adv. Manuf. Technol. 69 (2013) 211–223, https://doi.org/10.1007/s00170-013-4996-8.
[7] M. Bach, L. Degenkolb, F. Reuther, V. Psyk, R. Demuth, M. Werner, Conductive heating during press hardening by hot metal gas forming for curved complex Part Geometries, Metals 10 (2020) 1104, https://doi.org/10.3390/met10081104.
[8] T. Lin, H.-W. Song, S.-H. Zhang, M. Cheng, W.-J. Liu, Cooling systems design in hot stamping tools by a thermal-fluid-mechanical coupled approach, Adv. Mech. Eng. 6 (2014), https://doi.org/10.1155/2014/545727.
[9] H. Steinbeiss, H. So, T. Michelitsch, H. Hoffmann, Method for optimizing the cooling design of hot stamping tools, Prod. Eng. 1 (2007) 149–155, https://doi.org/10.1007/s11740-007-0010-3.
[10] AGK Hochleistungswerkstoffe GmbH, Thermische Trennung, 2022. https://www.agk.de/html/pressenisolation.htm.
[11] T. Maeno, K. Mori, R. Yachi, Hot stamping of high-strength aluminium alloy aircraft parts using quick heating, CIRP Ann 66 (2017) 269–272, https://doi.org/10.1016/j.cirp.2017.04.117.
[12] AGK Hochleistungswerkstoffe GmbH, AGK Werkstoffkatalog, 2022. https://www.agk.de/pdf/produkte/AGK_Werkstoffkatalog_DE.pdf.
[13] E.C. Walter, Pritzkow Spezialkeramik, Kennwerttabelle „Keramikblech", Oxidkeramischer Faserverbundwerkst. „Keramikblech", Übersicht, (Stand 2021), 2021. https://www.keramikblech.com/fileadmin/user_upload/pdf/01_Gesamttabelle_D_2021.pdf.
[14] L. Galdos, E. Sáenz de Argandoña, N. Herrero, A. Sukia, R. Ortubay, X. Agirretxe, J. Intxaurbe, Influence of tooling material and temperature on the final properties of tailor tempered boron steels, Key Eng. Mater. 611–612 (2014) 1102–1109. https://doi.org/10.4028/www.scientific.net/KEM.611-612.1102.
[15] R.A. Simon, R. Danzer, Oxide fiber composites with promising properties for high-temperature structural applications, Adv. Eng. Mater. 8 (2006) 1129–1134, https://doi.org/10.1002/adem.200600149.
[16] D.M. Wilson, L.R. Visser, High performance oxide fibers for metal and ceramic composites, Composites Part A Appl. Sci. Manuf. 32 (2001) 1143–1153, https://doi.org/10.1016/S1359-835X(00)00176-7.
[17] M.B. Ruggles-Wrenn, M.L. Harkins, To drill or not to drill? Creep of an oxide-oxide composite with diamond-drilled effusion holes at elevated temperature, Int. J. Appl. Ceram. Technol. (2022), https://doi.org/10.1111/ijac.14063.
[18] M.A. Mattoni, J.Y. Yang, C.G. Levi, F.W. Zok, L.P. Zawada, Effects of combustor rig exposure on a porous-matrix oxide composite, Int. J. Appl. Ceram. Technol. 2 (2005) 133–140, https://doi.org/10.1111/j.1744-7402.2005.02015.x.
[19] C.J. Armani, M.B. Ruggles-Wrenn, G.E. Fair, R.S. Hay, Creep of Nextel^{TM} 610 fiber at 1100°C in air and in steam, Int. J. Appl. Ceram. Technol. 10 (2013) 276–284, https://doi.org/10.1111/j.1744-7402.2012.02831.x.
[20] T.E. Steyer, Shaping the future of ceramics for aerospace applications, Int. J. Appl. Ceram. Technol. 10 (2013) 389–394, https://doi.org/10.1111/ijac.12069.
[21] N. Hannoschöck, Thermophysikalische stoffwerte, in: Wärmeleitung Und -Transport, Springer Berlin Heidelberg, Berlin, Heidelberg, 2018, pp. 423–492, https://doi.org/10.1007/978-3-662-57572-7.
[22] A. Hofenauer, R. Kirmeier, R. Markusch, H. Windsheimer, N. Travitzky, P. Greil, Verfahren zur Herstellung einer Keramik aus präkeramischen Papier- oder Pappstrukturen, 2018. DE 10 2006 022 598 B4.
[23] D. Nikolay, A. Hofenauer, C. Sorg, Ceramics produced by paper-processing technology, Keram. Z. 62 (2010) 191–196.
[24] T. Schlordt, B. Dermeik, V. Beil, M. Freihart, A. Hofenauer, N. Travitzky, P. Greil, Influence of calendering on the properties of paper-derived alumina ceramics, Ceram. Int. 40 (2014) 4917–4926, https://doi.org/10.1016/j.ceramint.2013.10.080.
[25] T. Wamser, W. Krenkel, G. Puchas, Keramische Verbundwerkstoffe und Verfahren zu ihrer Herstellung, 2016. WO2016016388A1 (2016).
[26] T. Wamser, W. Krenkel, G. Puchas, Keramische Verbundwerkstoffe und Verfahren zu ihrer Herstellung, 2017. WO2017220727A1 (2017).
[27] F. Lindner, G. Puchas, S. Schafföner, Novel measuring method for prepreg processability of oxide fiber ceramic matrix composites, Composites Part A Appl. Sci. Manuf. 162 (2022), 107131, https://doi.org/10.1016/j.compositesa.2022.107131.
[28] J. Winkelbauer, G. Puchas, W. Krenkel, S. Schafföner, Short fiber spraying process of all-oxide ceramic matrix composites: a parameter study, Int. J. Appl. Ceram. Technol. (2022), https://doi.org/10.1111/ijac.14196.
[29] L. Wagner, G. Puchas, W. Krenkel, S. Schafföner, Influence of matrix densification on the properties of weak matrix oxide fiber composites, Composites Part A Appl. Sci. Manuf. 164 (2023), 107274, https://doi.org/10.1016/j.compositesa.2022.107274.
[30] H. Li, F. Yang, B. xing Zhang, Y. Guo, W. Han, T. Zhao, W. Qiu, Preparation and characterization of Nextel 720/alumina ceramic matrix composites via an improved prepreg process, Int. J. Appl. Ceram. Technol. 19 (2022) 1970–1980, https://doi.org/10.1111/ijac.14037.
[31] H. Schneider, J. Schreuer, B. Hildmann, Structure and properties of mullite-A review, J. Eur. Ceram. Soc. 28 (2008) 329–344, https://doi.org/10.1016/j.jeurceramsoc.2007.03.017.
[32] M. Munro, Evaluated material properties for a sintered alpha-alumina, J. Am. Ceram. Soc. 80 (2005) 1919–1928, https://doi.org/10.1111/j.1151-2916.1997.tb03074.x.
[33] K.W. Schlichting, N.P. Padture, P.G. Klemens, Thermal conductivity of dense and porous yttria-stabilized zirconia, J. Mater. Sci. 36 (2001) 3003–3010, https://doi.org/10.1023/A:1017970924312.
[34] G. Puchas, S. Möckel, W. Krenkel, Novel prepreg manufacturing process for oxide fiber composites, J. Eur. Ceram. Soc. 40 (2020) 5930–5941, https://doi.org/10.1016/j.jeurceramsoc.2020.06.064.
[35] J. Winkelbauer, G. Puchas, S. Schafföner, W. Krenkel, Short fiber-reinforced oxide fiber composites, Int. J. Appl. Ceram. Technol. 19 (2022) 1136–1147, https://doi.org/10.1111/ijac.13931.
[36] F.W. Zok, Developments in oxide fiber composites, J. Am. Ceram. Soc. 89 (2006) 3309–3324, https://doi.org/10.1111/j.1551-2916.2006.01342.x.